



Mott insulators in moiré transition metal dichalcogenides at fractional fillings: Slave-rotor mean-field theory

Zhenhao Song ^{1,*}, Urban F. P. Seifert,² Zhu-Xi Luo,³ and Leon Balents ^{2,4}

¹*Department of Physics, University of California, Santa Barbara, California 93106, USA*

²*Kavli Institute for Theoretical Physics, University of California, Santa Barbara, California 93106, USA*

³*Department of Physics, Harvard University, Cambridge, Massachusetts 02138, USA*

⁴*Canadian Institute for Advanced Research, Toronto, Ontario, Canada*



(Received 25 July 2023; revised 15 September 2023; accepted 20 September 2023; published 6 October 2023)

In this work, we study a slave-rotor mean-field theory of an extended Hubbard model, applicable to transition metal dichalcogenide moiré systems, that captures both the formation of Wigner crystals as well as exotic spin states on top of these charge backgrounds. Phase diagrams are mapped out for different choices of long-range Coulomb repulsion strength, reproducing several experimentally found Wigner crystal states. Assuming unbroken time-reversal symmetry, we find several spin-liquid states as well as dimer states at fractional fillings. While spin dimer states are always found to have the lowest mean-field energy, several spin-liquid states are energetically competitive and may be stabilized by including gauge fluctuations or further interaction terms. We further discuss possible experimental signatures of these states pertinent to two-dimensional moiré heterostructures.

DOI: [10.1103/PhysRevB.108.155109](https://doi.org/10.1103/PhysRevB.108.155109)

I. INTRODUCTION

Moiré patterns are formed by two or more similar two-dimensional lattices overlaid with a slight relative strain or twist angle, giving rise to a large-scale periodic structure. The most prominent example, twisted bilayer graphene, theoretically proposed by Bistritzer and MacDonald [1], has been found to host a variety of strong correlation phenomena such as superconductivity and correlated insulating states [2,3]. Moiré systems often feature strongly quenched kinetic energy scales and flat bands such that electronic interactions become dominant, providing a fertile ground for exploring strong correlations in condensed matter systems. However, the flat band of twisted bilayer graphene is highly degenerate (spin and valley) and nonlocal [4], such that the validity of Hubbard-type models for localized orbitals is under debate.

On the other hand, moiré heterostructures constructed from transition metal dichalcogenides (TMDs) also exhibit flat bands, where only a twofold pseudospin degeneracy is present due to large spin-orbit coupling and resulting spin-valley locking in TMDs. Wannier centers constructed from the flat band of some moiré TMDs turn out to be localized at triangular superlattice sites, and thus effective moiré Hubbard model can be formulated [5,6]. Moiré TMDs are also insensitive to the precise magic angle, i.e., flatness is maintained for a large range of twist angles. These features, along with tunable filling via gating, make moiré TMDs an ideal and flexible platform to “simulate” [7,8] the Hubbard model and study novel phases that can emerge in systems of strongly correlated electrons [9]. Moreover, several moiré TMD systems are found to feature topologically nontrivial bands [10,11], hence

providing a platform to study the interplay of band topology and strong interactions [12,13].

Recent experiments on WSe₂/WS₂ moiré heterostructures as well as twisted WSe₂/WSe₂ homobilayers have demonstrated Mott-insulating states at half-filling, as well as correlated insulating states at various fractional fillings [14,15], corresponding to generalized Wigner crystals, where longer-ranged Coulomb interactions lead to the localization of charges on self-organized lattices.

A highly topical open problem in this context is concerned with possible magnetic states that would arise at lowest temperatures by interactions lifting the residual spin degeneracies of charges localized on lattice sites [5,9,16,17]. Since at some fractional fillings, the effective charge lattices correspond to frustrated lattices, these states may be prime candidates for the realization of highly sought-after quantum spin liquids [18,19], featuring long-range entanglement and fractionalized excitations, see also Fig. 1 for an illustration.

In this work, we focus on the moiré-Hubbard model with nearest-neighbor hopping t , onsite and longer-range Coulomb repulsions U and V_{ij} as an effective model for correlated electrons and holes on an emergent moiré triangular lattice, as applicable for K -valley moiré TMD heterostructures, such as WSe₂/WS₂ heterobilayers or twisted WSe₂ homobilayers [5,7,20]. In principle, given a particular charge-ordered configuration [stabilized by onsite (U) and longer-ranged (V_{ij}) repulsive interactions], one can perform a perturbative expansion in the hopping $t \ll U, V_{ij}$ to derive an effective strong-coupling Hamiltonian that lifts the spin degeneracy. However, this procedure is cumbersome in practice, requiring separate perturbative expansions for each filling factor. Further, at dilute fillings, spin-spin interactions may only be induced by processes at higher order in perturbation theory [17,21], and finding the ground states and phase diagrams of

*z_song@ucsb.edu

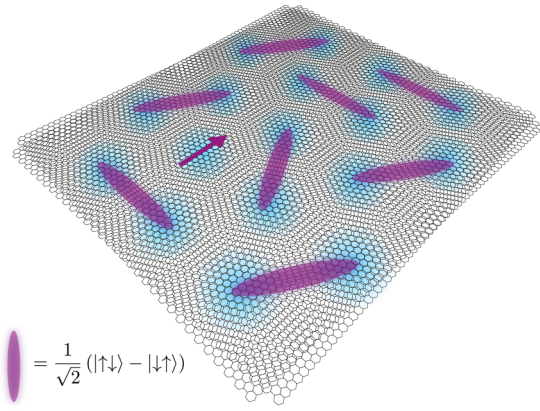


FIG. 1. Illustration of quantum magnetism in moiré transition metal dichalcogenides. At low energies, charged quasiparticles carry a pseudospin- $\frac{1}{2}$ degree of freedom. In incompressible phases (for example, at half-filling, pictured), the charge degrees of freedom (blue) become localized in Wannier orbitals of the moiré triangular lattice. The remaining spin degrees of freedom are frustrated, and quantum fluctuations can stabilize quantum spin-liquid states [for example, resonating valence bonds (RVB), illustrated with valence bonds in purple, supporting isolated spinons as fractionalized excitations] or nonmagnetic dimer states.

resulting spin Hamiltonians (often with multiple competing interactions) requires significant numerical efforts. Such a program was undertaken recently by Motruk *et al.* in Ref. [17], where an effective spin model for pseudospin- $\frac{1}{2}$ degrees of freedom in the kagome charge crystal (at filling $\frac{3}{4}$) was studied using density matrix renormalization group (DMRG) simulations, finding chiral spin-liquid and kagome spin-liquid phases.

In the paper at hand, we instead pursue a more integrated approach, aiming at a framework to simultaneously describe charge-ordered states at various fractional fillings and the concomitant magnetic states on top of these states. To this end, we employ a slave-rotor representation, first introduced by Florens and Georges [22]. In this representation, each electron is fractionalized into a fermionic spinon (carrying spin, but no charge) and an O(2) rotor degree of freedom, with its angular momentum corresponding to the electronic charge. Within the slave-rotor representation, the Hubbard model then becomes a model of interacting spinons and rotor degrees of freedom. Making a mean-field approximation, this interacting problem can be split into a solvable free-spinon Hamiltonian and a quantum XY model, with self-consistency equations coupling the two mean-field Hamiltonians.

Solving these self-consistency equations numerically allows us to map out phase diagrams, and characterize the nature of respective phases. We summarize our main results below:

(1) We find various incompressible (Mott-insulating) states with charges forming emergent honeycomb ($\bar{n} = \frac{4}{3}, \frac{5}{3}$ filling) and kagome ($\bar{n} = \frac{5}{4}, \frac{7}{4}$) Wigner crystals on the (moiré) triangular lattice, as observed in previous experiments [14]. These states are accessible by tuning chemical potential and/or the overall strength of repulsive electronic interactions (compared to kinetic energy scales).

(2) Distinct insulating states are separated by metallic (compressible) states, that are entered via first-order metal-insulator transitions. At fractional fillings, “partially metallic” states are found, where quasiparticles disperse on emergent lattices that are inherited from adjacent Wigner crystal phases, e.g., honeycomb or kagome sublattices of the triangular lattice.

(3) Considering incompressible (insulating) states, within our mean-field theory it is energetically preferable for the spinons to form dimerized states, corresponding to (possibly fluctuating) valence-bond solid (VBS) magnetic states that lift the remaining spin degeneracy of localized charges. We further find that some U(1) spin-liquid states are energetically competitive to these dimer states, such as 0-flux spinon Fermi surface U(1) spin liquid and staggered π -flux U(1) Dirac spin liquid on half-filling triangular charge crystal and $\frac{5}{4}$ filling kagome charge crystal. We discuss the stability of such U(1) spin-liquid states on these different charge crystals.

The outline of this paper is as follows. In Sec. II we briefly describe the generalized Hubbard model on the effective moiré triangular lattice, and detail the symmetry properties of the physical moiré system and the effective Hubbard model. In Sec. III, we introduce the slave-rotor representation and mean-field approximation, and describe the solution of self-consistent equations for the decoupled free fermion and rotor Hamiltonian. In Sec. IV, we discuss results of our mean-field calculation and present phase diagrams as a function of chemical potential and interaction strength. In Sec. V, we explore the physics beyond mean-field theory, give arguments on the stability of different spin liquids, and discuss possible experimental signatures. A summary and outlook is given in Sec. VI.

II. MOIRÉ-HUBBARD MODEL

A. Hamiltonian

In this work, we are concerned with the moiré-Hubbard model on an effective triangular lattice (on moiré lattice scales), with the Hamiltonian

$$H = H_t + H_U, \quad (1)$$

where

$$H_t = \varepsilon_0 \sum_{i,\sigma=\uparrow,\downarrow} c_{i,\sigma}^\dagger c_{i,\sigma} + \sum_{ij,\sigma=\uparrow,\downarrow} t_{ij,\sigma} c_{i,\sigma}^\dagger c_{j,\sigma}, \quad (2a)$$

$$H_U = \frac{U}{2} \sum_i (n_i - 1)^2 + \frac{1}{2} \sum_{ij} V_{ij} (n_i - 1)(n_j - 1). \quad (2b)$$

Here, ε_0 is the onsite energy, i, j denote lattice sites of the effective moiré triangular lattice, $t_{ij,\sigma}$ corresponds to a (possibly complex) spin-dependent hopping amplitude, U is the onsite Coulomb repulsion, and V_{ij} is the long-range Coulomb interaction. As discussed further below, we will mostly focus on truncating long-ranged Coulomb interaction to nearest neighbor V and next-nearest neighbor V' for simplicity, but write V_{ij} for generality. The total electron number $n_i = n_{i,\uparrow} + n_{i,\downarrow}$.

Note that we have defined the interaction term (2b) so that the interaction term is invariant under particle-hole transformations (while the kinetic energy is not). $\varepsilon_0 = 0$ corresponds

to half-filling when the hopping $t_{ij,\sigma}$ is zero. H_U is related (up to a constant) to the conventional form $U \sum_i n_{i,\uparrow} n_{i,\downarrow} + V \sum_{\langle ij \rangle} n_i n_j + V' \sum_{\langle\langle ij \rangle\rangle} n_i n_j$ by a redefinition of the onsite energy $\epsilon_0 \rightarrow \epsilon_0 - U/2 - 6(V + V')$.

As written, the Hamiltonian is agnostic regarding specific material realizations. A general principle that gives rise to such effective moiré-Hubbard Hamiltonians consists in determining the band structure that arise when holes near the valence-band maxima (VBM) experience a slowly varying periodic moiré potential (in heterobilayers, induced by a second layer with incommensurate lattice geometry), or a periodically varying interlayer hybridization (in twisted homobilayer systems). Considering nearly flat and well-isolated moiré bands, one may then construct appropriate localized Wannier orbitals, with their overlaps giving rise to the tight-binding dispersion H_t , and H_U is obtained from projecting Coulomb interactions onto these localized orbitals. The locations of the centers of these Wannier orbitals therefore determine the effective lattice geometry in Eq. (1). In TMDs with \mathbf{K} -valley VBM, strong spin-orbit coupling leads to a locking of spin and valley degrees of freedom near the Fermi level, so that quasiparticles in the effective moiré-Hubbard model carry a single (combined) $S_{\text{eff}} = \frac{1}{2}$ spin-valley degree of freedom (pseudospin).

We briefly discuss possible material realizations:

(1) Heterobilayers such as $\text{WSe}_2/\text{MoSe}_2$ [10] or WSe_2/WS_2 [7]: the topmost moiré band originates from the \mathbf{K}/\mathbf{K}' valley valence electrons of the WSe_2 layer, experiencing a triangular moiré potential modulated by the WS_2 or MoSe_2 layer. Wannier centers constructed from this moiré band are found to form an effective triangular lattice [20].

(2) Twisted homobilayers such as twisted bilayer WSe_2 [6,23]: the \mathbf{K}/\mathbf{K}' valley valence bands from both layers hybridize to generate the (topologically trivial) \mathbf{K}/\mathbf{K}' valley moiré bands, respectively. Wannier centers are found to form a triangular lattice, coinciding with sites in the moiré structure where the metal atoms in the two layers are aligned [5].

For both realizations, the topmost moiré bands are doubly degenerate and related to each other by time-reversal symmetry, corresponding to the pseudospin- $\frac{1}{2}$ degeneracy.

For some twisted TMDs, most prominently twisted bilayer MoTe_2 [10], Wannier states for the topmost moiré bands are found to form an effective honeycomb superlattice, with pseudospin- $\frac{1}{2}$ -dependent intralayer hopping giving rise to an effective realization of the Kane-Mele model. The interplay of band topology and strong interactions has recently received immense attention, following experimental reports of fractional quantum anomalous Hall states [12,13].

In the following, we will focus on moiré TMD systems well described by effective triangular Hubbard models, for which generalized Wigner crystal states have been observed experimentally [15]. We stress that, in principle, our slave-rotor mean-field study as presented in Sec. III can be straightforwardly applied to appropriate Kane-Mele-Hubbard models, which is an interesting avenue left for further study. However, we note that pseudospin-dependent complex next-nearest-neighbor hoppings give rise to Dyzalooshinskii-Moriya interactions in the strong-coupling limit which can be expected to stabilize (noncollinear) magnetic order rather than spin-liquid phases [9].

B. Symmetries

Moiré heterostructures have distinct microscopic symmetries. TMD monolayers possess C_{3v} symmetry, with a vertical reflection plane parallel to the links of the effective honeycomb lattice. For (*twisted*) *heterobilayers*, this reflection symmetry is broken, and the C_{3v} symmetry is reduced to a C_3 symmetry. *Twisted homobilayers* have D_3 symmetry which is generated by C_3 rotations as well as C_2 rotations around an in-plane axis which swaps the top and bottom layers. Note that vertical displacement field, e.g., introduced by gate voltages, would break the layer pseudospin symmetry and reduce it to a C_3 symmetry. For both systems, time-reversal symmetry is preserved, connecting the \mathbf{K} (spin-up) and \mathbf{K}' (spin-down) degrees of freedom.

The effective Hubbard model (1) is constructed by projecting the repulsive Coulomb interactions to the lowest-energy (flat) bands derived from continuum models for \mathbf{K} -valley moiré TMD [5,6]. Crucially, in Refs. [5,6] moiré potentials were truncated beyond the lowest harmonics (i.e., restricting to Fourier components corresponding to the first six moiré reciprocal lattice vectors). As we detail in Appendix A, this truncation leads to the emergence of an accidental inversion symmetry of the moiré-Bloch wave functions, and thus also of the effective Hubbard model for the respective Wannier states.

Now we comment on the validity of the lowest harmonics approximation, following the original argument in the Bistritzer-MacDonald paper [1] for twisted bilayer graphene. We expect the interlayer tunneling amplitude t_q at momentum q to drop rapidly on the reciprocal lattice vector scale. For example, based on Ref. [24], WSe_2 has interlayer separation $6.7 \text{ \AA} \leq d_{\perp} \leq 7.1 \text{ \AA}$, which exceeds the intralayer lattice constant $a = 3.28 \text{ \AA}$ by more than a factor of 2. Because the real-space hopping $t(\mathbf{r})$ varies with three-dimensional separation $\sqrt{d_{\perp}^2 + r^2}$, t_q decreases rapidly for $qd_{\perp} > 1$.

III. SLAVE-ROTOR MEAN-FIELD THEORY

We seek an integrated description of metal-insulator transitions (at zero temperature) and the concomitant formation of charge crystals at certain fractional fillings, and the magnetic states in the incompressible regimes (with localized charges). To this end, we employ a slave-rotor representation to explicitly separate the electrons' spin and charge degrees of freedom. While in an exact rewriting these are strongly coupled, we can make a mean-field approximation to obtain separate spin and charge Hamiltonians, coupled via self-consistency equations.

A. Slave-rotor representation

Following Ref. [22], we split electrons at each site into fermionic chargeless spinons and a single onsite $O(2)$ rotor degree of freedom. The rotor is used to represent the phase degree of freedom θ_i , conjugate to the total charge at site i , identified as the rotor's angular momentum $\hat{L}_i = -i\partial/\partial\theta_i$. The electron creation operator at site i is rewritten as

$$c_{i,\sigma}^{\dagger} = f_{i,\sigma}^{\dagger} e^{i\theta_i} \quad (3)$$

where the spinon $f_{i,\sigma}^\dagger$ has the same spin and orbit flavor as the electron, and $e^{i\theta_i}$ raises the angular momentum of the rotor by one unit. In other words, creating an electron amounts to creating a spinon and raising the angular momentum (total charge) by one at the same time. This rewriting enlarges the local Hilbert space and thus introduces redundant degrees of freedom. Therefore, a constraint is imposed that the number of spinons match the total charge,

$$\hat{L}_i = \sum_{\sigma} (f_{i,\sigma}^\dagger f_{i,\sigma} - 1/2). \quad (4)$$

Here, we choose the convention that the rotor quantum number $L_i = 0$ corresponds to half-filling, e.g., for electrons with spin $\frac{1}{2}$, $L_i = 0$ implies that there is exactly one electron at site i .

We note that the representation (3) is an exact rewriting if the constraint (4) is enforced on each site, for example, by means of a Gutzwiller projection. However, since there is only limited analytical understanding of projected wave functions, and their evaluation requires significant numerical efforts, we instead henceforth will enforce the constraint (4) *on average*. This approximation is equivalent to finding a saddle-point solution if we formulate it using a functional path integral. In this language the Lagrange multiplier can be seen to be equivalent to the temporal component of the emergent U(1) gauge field that couples to the spinons. Generalizing SU(2) to SU(N), it can be shown that the saddle-point solution becomes exact in the limit $N \rightarrow \infty$. The mean-field solution at a finite N has been benchmarked and compared to DMFT and the Gutzwiller approximation in Ref. [22], and can be expected to qualitatively capture the nature of different phases under the approximation.

The merit of the slave-rotor representation lies in the fact that Coulomb repulsion is only dependent on the charge quantum number, and we can thus replace the four-fermion interaction terms H_U [see Eq. (2b)] by terms quadratic in the rotor's angular momentum. Specifically, considering an atomic Hamiltonian with some onsite energy level ε_0 and onsite Coulomb repulsion U , we can write

$$\begin{aligned} H_{\text{at}} &= \sum_{\sigma} \varepsilon_0 c_{\sigma}^{\dagger} c_{\sigma} + \frac{U}{2} (n - 1)^2 \\ &= \sum_{\sigma} \varepsilon_0 f_{\sigma}^{\dagger} f_{\sigma} + \frac{U}{2} \hat{L}^2, \end{aligned} \quad (5)$$

where we drop an overall numerical constant. We now generalize to the Hubbard model in Eq. (1). Again using the slave-rotor representation in Eq. (3), and replacing $\hat{L}_i = n_i - 1$, the Hubbard Hamiltonian can be expressed in terms of spinons and rotors as

$$\begin{aligned} H &= - \sum_{i,\sigma} \mu f_{i,\sigma}^{\dagger} f_{i,\sigma} + \sum_i \frac{U}{2} \hat{L}_i^2 + \frac{1}{2} \sum_{ij} V_{ij} \hat{L}_i \hat{L}_j \\ &\quad - \sum_{ij,\sigma} t_{ij,\sigma} f_{i,\sigma}^{\dagger} f_{j,\sigma} e^{i(\theta_i - \theta_j)}. \end{aligned} \quad (6)$$

Here, we have replaced the onsite energy ε_0 by a chemical potential

$$\varepsilon_0 = -\mu, \quad (7)$$

which is an experimentally accessible tuning parameter (via electrostatic gating) [7]. In the following, we will therefore work in the grand-canonical ensemble rather than at fixed particle number.

The kinetic term of the Hubbard model has become a coupling between spinon and rotor degrees of freedom in Eq. (6). In principle, the constraint (4) should be imposed on each site.

B. Mean-field decoupling of spinons and charge rotors

The fermionic spinons and rotor degrees of freedom interact via the ‘‘correlated hopping’’ in Eq. (6), preventing an exact solution of the model. To make progress, here we perform a mean-field decoupling of the interaction term

$$\begin{aligned} f_{i,\sigma}^{\dagger} f_{j,\sigma}^{\dagger} e^{i(\theta_i - \theta_j)} &\rightarrow \langle f_{i,\sigma}^{\dagger} f_{j,\sigma}^{\dagger} \rangle e^{i(\theta_i - \theta_j)} + f_{i,\sigma}^{\dagger} f_{j,\sigma}^{\dagger} \langle e^{i(\theta_i - \theta_j)} \rangle \\ &\quad - \langle f_{i,\sigma}^{\dagger} f_{j,\sigma}^{\dagger} \rangle \langle e^{i(\theta_i - \theta_j)} \rangle, \end{aligned} \quad (8)$$

where $\langle \dots \rangle$ denotes an expectation value with respect to the ground state of the respective mean-field Hamiltonian.

We also add a Lagrange multiplier field h_i to impose the constraint (4). The Hamiltonian (6) then splits into separate Hamiltonians for the fermionic spinons and O(2) quantum rotors,

$$H_f = \sum_{i,\sigma} (-\mu - h_i) f_{i,\sigma}^{\dagger} f_{i,\sigma} - \sum_{ij,\sigma} t_{ij,\sigma}^{\text{eff}} f_{i,\sigma}^{\dagger} f_{j,\sigma}, \quad (9)$$

$$H_{\theta} = \sum_i \frac{U}{2} \hat{L}_i^2 + h_i \hat{L}_i + \sum_{ij} \frac{1}{2} V_{ij} \hat{L}_i \hat{L}_j - K_{ij} e^{i(\theta_i - \theta_j)}, \quad (10)$$

where the effective hopping $t_{ij,\sigma}^{\text{eff}}$ for the (free-) fermionic spinons and the coupling of quantum rotors K_{ij} are related to the mean-field parameters, and are to be determined self-consistently. Explicitly, the coupled self-consistency relations read as

$$t_{ij,\sigma}^{\text{eff}} = t_{ij,\sigma} \langle e^{i(\theta_i - \theta_j)} \rangle, \quad (11)$$

$$K_{ij} = \sum_{\sigma} t_{ij,\sigma} \langle f_{i,\sigma}^{\dagger} f_{j,\sigma} \rangle. \quad (12)$$

Further, the parameters h_i must be (implicitly) determined to satisfy the average constraint for matching the filling of spinons to each site's charge,

$$\langle \hat{L}_i \rangle = \sum_{\sigma} [\langle f_{i,\sigma}^{\dagger} f_{i,\sigma} \rangle - 1/2]. \quad (13)$$

C. Solution of rotor Hamiltonians

While the free-fermion Hamiltonian is easily diagonalized by means of a unitary transformation in momentum space, the Hamiltonian H_{θ} of interacting O(2) rotors (i.e., a *quantum XY* model) evades such an exact solution.

Instead, we will make physically motivated approximations to the rotor correlation expectation value $\langle e^{i(\theta_i - \theta_j)} \rangle$ which characterizes distinct phases of the quantum XY model, and in the present context then determine the effective spinon dispersion. We discuss two distinct regimes below.

1. Metallic (compressible) states

The rotor acquiring a nonzero expectation value $\langle e^{i\theta_i} \rangle \equiv \sqrt{Z}_i \neq 0$ can be understood to be analogous to the

condensation of a bosonic ladder operator $\langle b_i^\dagger \rangle$, giving rise to a superfluid phase for the bosonic degrees of freedom. This phase is characterized by off-diagonal long-range order of the rotor correlator at long distances, i.e., $\lim_{|i-j| \rightarrow \infty} \langle e^{i(\theta_i - \theta_j)} \rangle = \langle e^{i\theta_i} \rangle \langle e^{-i\theta_j} \rangle$. We can access this phase on a mean-field level by factorizing the correlator $\langle e^{i(\theta_i - \theta_j)} \rangle \approx \langle e^{i\theta_i} \rangle \langle e^{-i\theta_j} \rangle$. This implies that the effective spinon hopping [cf. Eq. (11)] can be written as

$$\begin{aligned} t_{ij,\sigma}^{\text{eff}} &= t_{ij\sigma} \langle e^{i\theta_i} \rangle \langle e^{-i\theta_j} \rangle \\ &= t_{ij\sigma} \sqrt{Z_i} \sqrt{Z_j}, \end{aligned} \quad (14)$$

where we assume $\langle e^{i\theta_i} \rangle$ is real, which should be expected if the time-reversal symmetry is unbroken, and then $\langle e^{i\theta_i} \rangle = \langle e^{-i\theta_i} \rangle = \sqrt{Z_i}$ from Hermiticity. The notation $\sqrt{Z_i}$ is used so that Z_i would have the meaning of spectral weight (see below). The nonzero expectation value of the phase operator indicates that the rotor's angular momentum, and thereby the electronic charge, is no longer a good quantum number and thus the system is in a metallic (compressible) state. Especially at commensurate fillings, upon increasing Coulomb repulsion, Z_i decreases continuously to zero, which is the well-known Mott transition as demonstrated in Ref. [22].

Within the slave-rotor formalism, the electronic Green's function $G^{(c)}$ is given by

$$G_{ij}^{(c)}(\tau - \tau') = G_{ij}^{(f)}(\tau - \tau') \langle e^{-i[\theta_i(\tau) - \theta_j(\tau')] } \rangle. \quad (15)$$

In the metallic states, the rotor degrees of freedom are long-range ordered, and in the mean-field approximation we can read off the spectral weights of the electronic quasiparticles as $Z_{ij} = \sqrt{Z_i} \sqrt{Z_j}$ where $\sqrt{Z_i} = \langle e^{i\theta_i} \rangle$. Note that here, the spinon bands contribute unity spectral weight, such that the wavefunction renormalization of the electronic quasiparticles is determined by the rotor degrees of freedom.

To explicitly solve the self-consistency equations, we note that with Eq. (14), the rotor Hamiltonian (10) can be written as

$$\begin{aligned} H_\theta &\approx \frac{U}{2} \sum_i \hat{L}_i^2 + \frac{1}{2} \sum_{ij} V_{ij} \hat{L}_i \hat{L}_j + \sum_i h_i \hat{L}_i \\ &\quad - \sum_i \left(\sum_j K_{ij} \sqrt{Z_j} \right) (e^{i\theta_i} + e^{-i\theta_i}) + \text{const.} \end{aligned} \quad (16)$$

In line with our site-factorized treatment of the rotor kinetic energy, we also decouple the long-range Coulomb interaction as

$$\sum_{ij} V_{ij} \hat{L}_i \hat{L}_j \approx \sum_{ij} V_{ij} (\hat{L}_i \langle \hat{L}_j \rangle + \langle \hat{L}_i \rangle \hat{L}_j - \langle \hat{L}_i \rangle \langle \hat{L}_j \rangle). \quad (17)$$

Then, the rotor Hamiltonian can be reduced to a sum of decoupled single-site rotor (mean-field) Hamiltonians

$$\begin{aligned} H_\theta^{\text{MF}} &= \sum_i \left[\frac{U}{2} \hat{L}_i^2 + \left(\sum_j V_{ij} \langle \hat{L}_j \rangle + h_i \right) \hat{L}_i \right] \\ &\quad - \sum_i \left(\sum_j K_{ij} \sqrt{Z_j} \right) (e^{i\theta_i} + e^{-i\theta_i}) + \text{const.} \end{aligned} \quad (18)$$

Given a set of K_{ij} , the mean-field Hamiltonian H_θ^{MF} can now be readily solved, where $\langle \hat{L}_i \rangle$ and $\sqrt{Z_i}$ are to be determined self-consistently: the corresponding ground-state expectation values $\langle e^{i\theta_i} \rangle$ then determine $t_{ij,\sigma}^{\text{eff}}$, which serves as an input for the solution of the fermionic spinon Hamiltonian, to obtain the value of K_{ij} for the next iteration.

2. Insulating (incompressible) states

We characterize insulating states by vanishing of the respective quasiparticle weights which attains when the phase operator expectation values $\langle e^{i\theta_i} \rangle = 0$. In this case, L would be quantized to be integers, giving rise to zero compressibility $\partial n / \partial \mu = 0$. When $\langle e^{i\theta_i} \rangle = \sqrt{Z_i} = 0$, there is no long-range order for the rotor degrees of freedom, but we stress that this does not necessarily lead to $\langle e^{i(\theta_i - \theta_j)} \rangle = 0$: A simple site-factorized mean-field treatment of the quantum XY model (as suggested for metallic states above) is incapable of correctly producing such finite (short-range) rotor correlations. Instead, we obtain the expectation value of this operator from Eq. (10) by the Hellmann-Feynman theorem

$$\langle e^{i(\theta_i - \theta_j)} \rangle = - \frac{\partial \langle H_\theta \rangle}{\partial K_{ij}}, \quad (19)$$

which makes explicit that, in general, rotor correlations do not vanish since the energy expectation value will depend on K_{ij} . This implies that in insulating states with vanishing quasiparticle weights $Z = 0$, the spinon in general still has nonzero hopping and disperses. Such spin-charge separation is typical of spin liquids.

In this work, we employ canonical perturbation theory to calculate the ground-state energy $\langle H_\theta \rangle$ of the rotor Hamiltonian (10) and the rotor correlation from Eq. (19) when the onsite mean fields $\langle e^{i\theta_i} \rangle = 0$ vanish. This perturbative expansion is controlled if the rotor-rotor coupling K_{ij} is small compared to the repulsive U, V interactions. To this end, we take the (solvable) Hamiltonian for the angular momenta as the unperturbed Hamiltonian

$$H_\theta^{(0)} = \sum_i \frac{U}{2} \hat{L}_i^2 + \frac{1}{2} \sum_{ij} V_{ij} \hat{L}_i \hat{L}_j + \sum_i h_i \hat{L}_i, \quad (20)$$

with the perturbation

$$H_\theta' = \sum_i \delta h_i \hat{L}_i - \sum_{ij} K_{ij} e^{i(\theta_i - \theta_j)}, \quad (21)$$

where we included δh_i as a possible change of Lagrange multipliers to ensure the constraint (13) remains satisfied. Then, the ground-state energy up to second order in K/U reads as

$$E_0 = E_0^{(0)} + \sum_i \delta h_i \langle L_i \rangle + \sum_{ij} \frac{K_{ij} K_{ji}}{E_0^{(0)} - E_{ij}^{(0)}} + O[(K/U)^3]. \quad (22)$$

Here, $E_{ij}^{(0)}$ corresponds to the energy of the configuration that one unit charge is moved from site j to site i , with respect to the unperturbed ground configuration. From Eq. (19) we can see that $\langle e^{i(\theta_i - \theta_j)} \rangle$ and thus $t_{ij,\sigma}^{\text{eff}}$ would be proportional to K_{ij} to the lowest order.

Equations (19) and (22) correspond to a set of self-consistent equations, now accounting for perturbative corrections. From these we can solve for \tilde{K}_{ij} and other parameters. There is always a trivial solution $K_{ij} = 0$, which is the normal insulating state. When $K_{ij} \neq 0$, we get nonzero spinon hoppings, while the system is still incompressible because the charge is quantized and conserved ($\langle e^{i\theta} \rangle = 0$).

3. Classification of spin-liquid states

When the \tilde{K}_{ij} are not zero in insulating states, we can get a larger set of solutions than the metallic case, which fall into different universality classes of spin liquids. In fact, in the decomposition (3), we have a U(1) gauge redundancy

$$\begin{aligned} f_{i,\sigma}^\dagger &\rightarrow e^{-i\varphi_i} f_{i,\sigma}^\dagger, \\ \theta_i &\rightarrow \theta_i + \varphi_i. \end{aligned} \quad (23)$$

After this transformation, the electron operators and thus the *physical* Hamiltonian remain invariant. However, given mean-field Hamiltonians H_f and H_θ will in general not be invariant under these transformations. Equivalently, one observes that even though a physical wave function for a spin liquid may preserve all physical symmetries (space-group symmetries, spin-rotation symmetry, and time-reversal symmetry), a corresponding mean-field Hamiltonian is only invariant if those symmetry operations are supplemented by appropriate gauge transformations as in Eq. (23). In other words, symmetries of mean-field *Ansätze* are realized projectively. Mean-field *Ansätze* corresponding to distinct physical states can be classified by their respective projective symmetry groups (PSG), as introduced in Ref. [25].

To be more explicit, consider a space-group transformation U under which the physical state $|\Psi_{\text{phys}}\rangle$ is invariant. Before projection, the mean-field state $|\Psi^{(K_{ij})}\rangle$ may not transform trivially under U since K_{ij} and K'_{ij} related by a U(1) gauge transformation [Eq. (23)] correspond to actually the same physical state. Invariance of the mean-field *Ansatz* K_{ij} is achieved by combining U with a U(1) gauge transformation

$$G_U U(K_{ij}) = K_{ij}, \quad (24)$$

where the physical operation U maps the spatial index i to some other index $U(i)$, and G_U is an appropriately chosen U(1) gauge transformation,

$$\begin{aligned} G_U : f_{i\sigma}^\dagger &\rightarrow e^{-i\varphi_{U(i)}} f_{i\sigma}^\dagger, \\ e^{i\theta_i} &\rightarrow e^{i\varphi_{U(i)}} e^{i\theta_i}, \\ K_{ij} &\rightarrow e^{-i(\varphi_{U(i)} - \varphi_{U(j)})} K_{ij}, \\ t_{ij,\sigma}^{\text{eff}} &\rightarrow e^{i(\varphi_{U(i)} - \varphi_{U(j)})} t_{ij,\sigma}^{\text{eff}}. \end{aligned} \quad (25)$$

The set of $G_U U$ that leaves K_{ij} invariant is referred to as the invariant PSG. Different PSG entail distinct K_{ij} *Ansätze*, and thus we can classify the mean-field *Ansätze* and corresponding *physical* states by their PSG realizations.

The subgroup of invariant PSG that is a pure gauge group is called invariant gauge group (IGG), and the physical sym-

metry group is hence given by $\text{SG} = \text{PSG}/\text{IGG}$. Here in the insulating case, a global U(1) transformation leaves K_{ij} and $t_{ij,\sigma}^{\text{eff}}$ invariant

$$\begin{aligned} f_{i,\sigma}^\dagger &\rightarrow e^{-i\varphi} f_{i,\sigma}^\dagger, \\ e^{i\theta_i} &\rightarrow e^{i\varphi} e^{i\theta_i}, \end{aligned} \quad (26)$$

where φ is site independent. Therefore, the slave-rotor representation has a U(1) IGG.

Then, we can ask how many gauge-inequivalent classes of spin liquids are allowed if we demand the full physical symmetry. The structure of the symmetry group imposes an algebraic constraint on the PSG. For example, demanding that translations along the two principal axes of a lattice commute implies

$$T_1^{-1} T_2 T_1 T_2^{-1} = \mathcal{I}. \quad (27)$$

Then, the PSG (24) with a U(1) IGG should satisfy

$$(G_{T_1} T_1)^{-1} G_{T_2} T_2 G_{T_1} T_1 (G_{T_2} T_2)^{-1} = G \in \text{U}(1). \quad (28)$$

The identity of the right-hand side of Eq. (27) is now relaxed to an element of U(1) IGG since it keeps the mean-field *Ansätze* invariant. Listing out all the relations of the symmetry group, we can get a finite number of distinct PSGs allowed by these algebraic constraints, called algebraic PSG. Since *Ansätze* K_{ij} are distinguished by their PSG realizations, we arrive at a finite number of choices, which are not related to each other by a pure gauge transformation, and thus fall into different classes. We can therefore focus on particular mean-field *Ansätze* K_{ij} that correspond to distinct PSG, under a given symmetry requirement.

Above arguments and PSG classifications in general employ the full symmetry group of the lattice on which spin degrees of freedom reside. However, in this work, we are in particular focused on charge-ordered states that may form in the generalized Hubbard model. At fractional fillings, charges then reside on effective sublattices of the triangular lattice (e.g., honeycomb lattice at $\frac{4}{3}$ filling or kagome lattice at $\frac{5}{4}$ filling). For these states, a similar PSG analysis can be applied based on the symmetry groups of the respective charge-ordered states (that spontaneously break translational and rotational symmetries of the parent triangular lattice). Moreover, if we allow a breaking of rotational symmetry, nematic states are possible, where the amplitudes of K_{ij} differ on bonds of different orientation. These also include dimer states that are formed if all the nonzero K_{ij} bonds are disconnected, corresponding to VBS states.

In the following, based on the discussion above, we will consider distinct invariant PSG *Ansätze* that have previously been found to be energetically competitive on various charge crystals, solve the self-consistent equations, respectively, and compare their respective energies.

We mention that also in the metallic phase, the slave-rotor Hamiltonian before mean-field decoupling formally enjoys a U(1) gauge redundancy. But the phase operator $e^{i\theta} \rightarrow \langle e^{i\theta} \rangle \neq 0$ acquiring a finite expectation value implies that the IGG here is just a trivial group with identity as the only element because $\langle e^{i\theta} \rangle$ would change under any transformation $\theta_i \rightarrow \theta_i + \phi_i$. This trivial IGG will result in only one solution allowed where

K_{ij} are the same on all bonds (a uniform solution), if the full physical symmetry is preserved: This metallic state does not possess an intrinsic gauge structure and corresponds to a confining phase.

We further note that dimer states which have $\langle f_{i,\sigma}^\dagger f_{j,\sigma}^\dagger \rangle \neq 0$ on disjoint bonds $\langle ij \rangle$ possess *on the mean-field level* a U(1) IGG. However, the disconnected nature of the spinon hopping, all fermionic degrees of freedom are gapped (i.e., spinons are localized on bonds, forming spin singlets after projection). Pure (compact) U(1) gauge theory in 2+1 dimensions is unstable [26,27], and thus the dimer phase must be a confining phase of matter.

IV. MEAN-FIELD PHASES

A. Overview

To map out phase diagrams, we numerically solve the self-consistency equations (11) and (12) in Sec. III B, as a function of chemical potential μ and interaction strength U . We find that phase diagrams depend significantly on the presence and nature of longer-ranged repulsive interactions V_{ij} in Eq. (2b) due to Coulomb interactions between charges.

Typically, the Coulomb interaction in bulk solids is efficiently screened (leading to an exponential decay with distance), justifying the approximation of repulsive interactions as an onsite (contact) interaction. However, in two-dimensional moiré heterostructures, screening is significantly weaker, and the moiré-induced quenching of kinetic energy scales implies that extended repulsive interactions are no longer negligibly small [28]. As we shall see below (and discuss in Appendix B), extended repulsive interactions (beyond nearest neighbor) are necessary for reproducing some of the more complex generalized Wigner crystals at certain filling factors.

In fact, the screening length in moiré TMD heterostructures can be controlled via the choice of and distance to metallic screening layers (which also act as gate electrodes). Modeling the screening via the method of image charges, the electron-electron interaction potential is $U(r) = (e^2/\epsilon)[r^{-1} - (r^2 + D^2)^{-1/2}]$, where D is the vertical distance between the metallic layer and TMD bilayer [20].

With this in mind, in this study, we for simplicity consider two distinct cases of next-nearest-neighbor repulsion V' :

(1) $V' = 0$, corresponding to short-ranged (truncated beyond nearest-neighbor repulsion V) interactions due to strong screening;

(2) $V' = \frac{1}{\sqrt{3}}V$, roughly motivated by a $1/r$ decaying Coulomb repulsion, such that V'/V is inversely proportional to distance ratio.

In both cases, we neglect repulsions beyond next-nearest neighbors for simplicity, and the ratio of nearest neighbor to onsite Coulomb repulsion V/U is fixed to be $\frac{1}{4}$ [5,29,30]. We expect that in realistic systems, V'/V should take a value between the two cases discussed above, depending on microscopic details. Note that here we also drop hopping amplitudes beyond nearest neighbors since the Wannier states on the moiré lattice scale are exponentially localized, and accordingly longer-ranged hopping has been found to be negligible compared to the strong Coulomb interactions in moiré TMDs [29,30]. Considering only nearest-neighbor

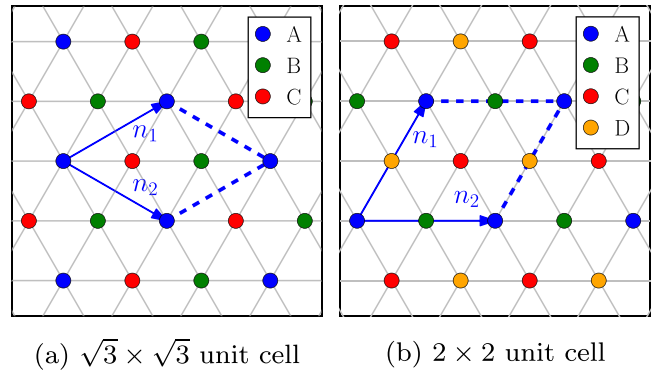


FIG. 2. Unit cells for three-site *Ansatz* and four-site *Ansatz*.

repulsion, a classical analysis shows that all possible charge crystals on the triangular have at most three distinct sublattices, so three inequivalent sublattice sites with possibly different L_i , Z_i , and h_i are needed, assuming a translational symmetry with respect to $\sqrt{3} \times \sqrt{3}$ unit cells [Fig. 2(a)]. On the other hand, if next-nearest-neighbor repulsion is included, charge-ordering patterns with four-site unit cells [Fig. 2(b)] become energetically competitive, allowing for striped phases and kagome-type effective sublattice charge order. In our numerical solutions of the self-consistency equations we consider various *Ansätze* in three- and four-site unit cells, and compare their respective total energies per site to determine the global ground state.

For simplicity, we restrict our analysis to the half-plane of $\mu > 0$ so that in our convention, the filling factor (mean number of particles per site) $\bar{n} \geq 1$ [i.e., hole-doped scenario since charged particles correspond to holes from the (K/K') valley in the monolayer TMDs [6,7,10,23]]. While the triangular lattice is not particle-hole symmetric, and thus the location of phases and phase boundaries may change, it is expected that for each generalized Wigner crystal at filling \bar{n} there will exist a “conjugate” phase at filling $2 - \bar{n}$.

We solve the mean-field self-consistency equations using an iterative procedure. We work on discretized momentum-space grids with 30×30 unit cells for both the three- and four-site *Ansätze*. The free-fermion Hamiltonian can be diagonalized easily in momentum space, with negligible finite-size effects. To solve the rotor Hamiltonian, we truncate the local rotor Hilbert space (which is in principle unbounded) to finite dimension with $L_{\min} = -5$ to $L_{\max} = 5$. This truncation is justified since states with large L would be suppressed by U , and we explicitly confirm its validity by noting that Z is close to 1 when $U = 0$ and $\varepsilon = 0$, as expected. We further note that this consideration also implies that the slave-rotor mean-field approach works better for a relatively large U .

We work in units of the kinetic energy t , and employ a small but finite temperature $k_B T/t = 0.01$ for numerical stability. Here, the Fermi distribution function is used as a smooth function to avoid numerical instabilities. Note that strictly speaking, at finite temperatures, the ground-state minimizes the free energy $F = E - TS$ (rather than E), but we have checked that our results (comparing E of different states) remain invariant when using finite temperatures on the order of $T = 10^{-4}t$ to $T = 0.01t$. Hence, we expect the results

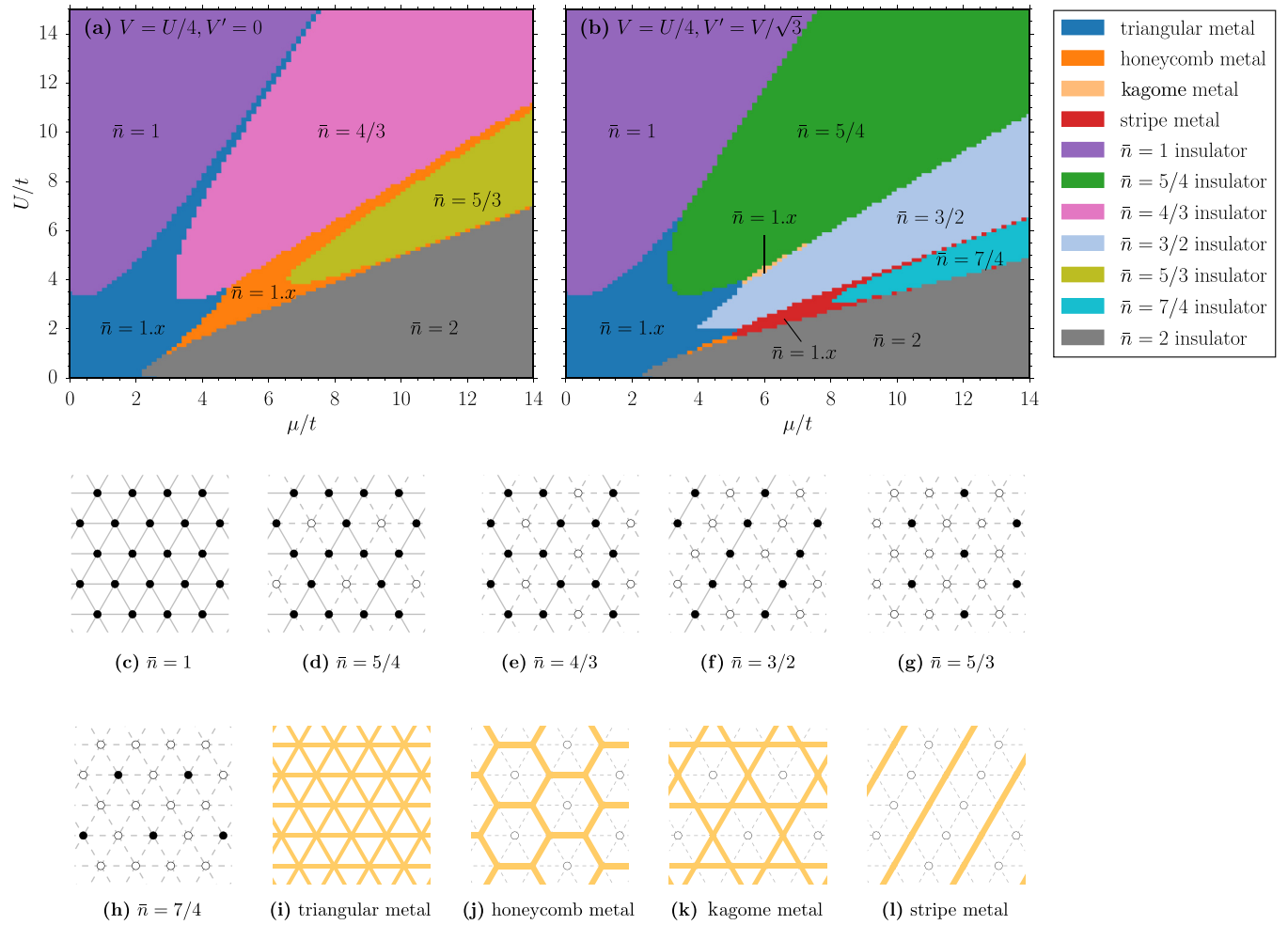


FIG. 3. Mean-field phase diagrams in the μ - U plane, for nearest-neighbor repulsion $V = U/4$, and two representative values of next-nearest-neighbor repulsion V' , (a) $V' = 0$ and (b) $V' = V/\sqrt{3}$. Average particle number \bar{n} is a commensurate fractional number for insulating phases, and $\bar{n} = 1.x$ denotes incommensurate filling for metallic states conducting on different sublattices. (c)–(f) Schematic depiction of various charge orders (corresponding to generalized Wigner crystals) found for correlated insulating states at fractional filling. Filled and empty circles correspond to half-filled and doubly occupied sites. On solid lines spinons may have nonzero hopping, whereas bonds denoted by dashed lines do not contribute to the connectivity of the lattice. (i)–(l) Schematic depiction of metallic states, with charges dispersing on different sublattices of the parent moiré triangular lattice. Orange shading indicates bonds on which charges disperse, and empty circles correspond to doubly occupied sites.

calculated at $T = 0.01t$ to reflect the energetic competition of states at zero temperature.

The mean-field phase diagrams in the plane of U and μ (in units of t) for short-range repulsion $V' = 0$ is shown in Fig. 3(a), and for longer-ranged repulsion $V' = \frac{1}{\sqrt{3}}V$ in Fig. 3(b). Various charge crystal states are illustrated in Figs. 3(c)–3(h), and metallic states with charge dispersion on distinct sublattices in Figs. 3(i)–3(l).

Depending on V' , we find distinct charge-ordering patterns: For $V' = 0$, there are emergent honeycomb Wigner crystals at $\frac{4}{3}$ and $\frac{5}{3}$ filling [Figs. 3(e) and 3(g)] as well as half-filling [Fig. 3(c)]. These Mott-insulating states are separated by metallic states conducting on an emergent honeycomb sublattice [Fig. 3(j)] or parent triangular lattice [Fig. 3(i)]. On the other hand, for $V' = \frac{1}{\sqrt{3}}V$, charge orders of kagome type at $\frac{5}{4}$ and $\frac{7}{4}$ filling [Figs. 3(d) and 3(h)] and stripe type at $\frac{3}{2}$ filling [Fig. 3(f)] are more favored than order with $\sqrt{3} \times \sqrt{3}$

periodicity. These states are accompanied by metallic states dispersing on respective sublattices [Figs. 3(k) and 3(l)].

States of commensurate fractional fillings in the phase diagrams are all insulators with $\sqrt{Z}_i = 0$, and the compressibility $\partial n/\partial \mu = 0$ because the charge per site n_i is quantized in a range of chemical potential μ . In these parameter regimes, we use perturbation theory in K/U in order to obtain finite (short-ranged) spin correlations determined by $\langle e^{i(\theta_i - \theta_j)} \rangle$ as introduced in Sec. III C 2, with details discussed in the following subsections.

When some of the $\langle e^{i\theta_i} \rangle \neq 0$, there is a finite quasiparticle weight and the system is in a compressible metallic state [corresponding to incommensurate particle numbers in the phase diagram Figs. 3(a) and 3(b)]. In addition to the metallic state corresponding to particles dispersing on the triangular lattice (with uniform $\langle e^{i\theta_i} \rangle \neq 0$), we also find states where particles disperse on a honeycomb sublattice formed by two of the three sites in the $\sqrt{3} \times \sqrt{3}$ unit cell, and kagome or

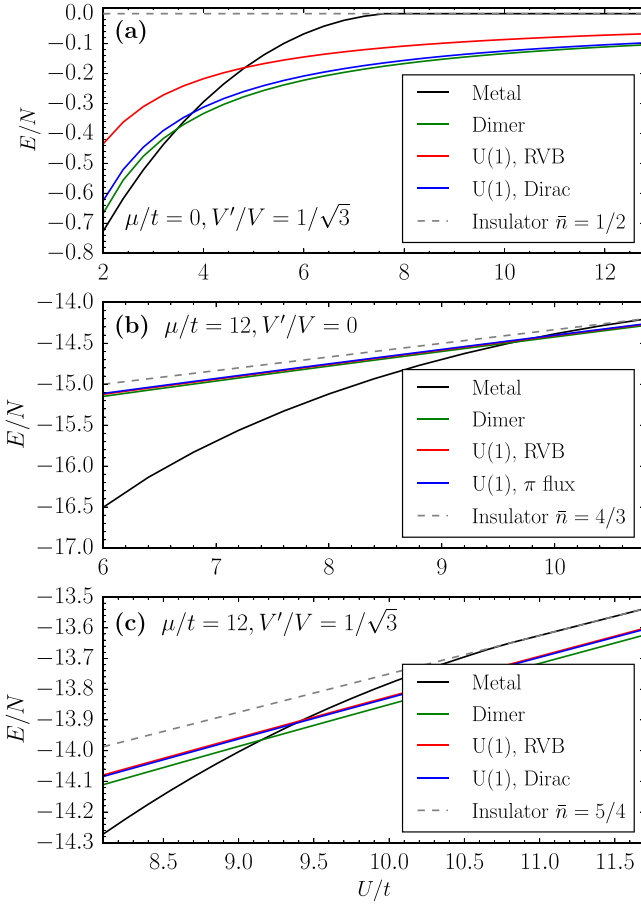


FIG. 4. Energy per site E/N as a function of U/t for different candidate states on different Wigner crystals. Note that here, we explicitly enforce particular charge crystals [i.e., these plots do *not* correspond to cuts through the phase diagrams in Figs. 3(a) and 3(b)] in order to study the competition of various spinon *Ansatz* states. (a) Triangular charge crystal (with $\bar{n} = 1$), (b) honeycomb charge crystal (with $\bar{n} = \frac{4}{3}$), (c) kagome charge crystal ($\bar{n} = \frac{5}{4}$). The dashed lines indicate the energy of “trivial” insulating states without any spinon hopping. And the black solid lines correspond to metallic states living on sublattices of respective charge orders, i.e., (a) triangular, (b) honeycomb, and (c) kagome metal phase.

stripe sublattices formed by three or two sites in the 2×2 unit cell, while the remaining site is doubly occupied, leading to $\langle e^{i\theta_i} \rangle = 0$ for the corresponding i . The metallic states conducting on different sublattices are sketched in Figs. 3(i)–3(l). While the uniformly dispersing metallic state on the parent triangular lattice is present in both phase diagrams of $V' = 0$ and $\frac{1}{\sqrt{3}}V$, the honeycomb metal is only favored for $V' = 0$, and the kagome and stripe metals are more competitive in the latter case.

At a fixed chemical potential, upon increasing interaction strength U (simultaneously also increasing V , V' proportionally), the metallic state enters an adjacent insulating charge-ordered state through a first-order phase transition, in contrast to a continuous Mott transition with a spectral weight going to 0, as also shown in Fig. 4 in next subsection. The critical U for a continuous Mott transition is marked by the vanishing of the quasiparticle weights Z_i and can be obtained

by applying a perturbative approximation on Z_i , as shown in Ref. [22]. From Eq. (16), and making use of Hellmann-Feynman theorem, we have

$$\sqrt{Z_i} \equiv \langle e^{i\theta_i} \rangle = \frac{4U\sqrt{Z_i}\tilde{K}_i}{U^2 - 4(U L_i + \sum_j V_{ij} L_j + h_i)^2} \quad (29)$$

where $\tilde{K}_i = \sum_{j \in \text{nn}(i)} K_{ij}$ is the sum over nearest sites in the corresponding metallic sublattice (since we are keeping only nearest hoppings). At the boundary of the insulating state, $h_i = \epsilon_0 = -\mu$ to satisfy the constraint Eq. (4). Eliminating Z_i on both sides, we get an equation of the critical interaction strength U_C and V_{ijC} .

$$U_C^2 - 4 \left(U_C L_i + \sum_j V_{ijC} L_j - \mu \right)^2 = 4\tilde{K}_i U_C \quad (30)$$

The value of \tilde{K}_i can be calculated from the self-consistency equation Eq. (12), which would be independent on $\sqrt{Z_i}$ if the non-zero $\sqrt{Z_i}$ is uniform on corresponding sublattices with $h = -\mu$ near transition.

B. Spin liquids and dimerized states in insulating phases

When all $\sqrt{Z_i} = 0$, all electronic quasiparticle weights vanish and thus the system enters an insulating regime. Distinct insulating states (at identical filling and charge order) can be characterized by their corresponding spin states. Focusing on nonmagnetic states such as spin liquids and dimer states, as stated in Secs. III C 2 and III C 3, the mean-field parameters K_{ij} will generically be nonzero and can be used to classify various *Ansatz* states corresponding to their respective invariant PSG.

In the following, we analyze self-consistent solutions to the mean-field equations corresponding to symmetry-allowed spin-liquid states, as well as dimerized solutions. While we find that for all insulating states the dimerized state always has the lowest energy in our mean-field calculation (with perturbative corrections), various spin-liquid states are competitive in energy with respect to the mean-field Hamiltonian.

1. Triangular charge crystal (half-filling)

At half-filling, every site of the moiré triangular lattice is occupied by one charge ($L_i = 0$). While charges are localized to sites, spinons can hop on the triangular lattice with nonzero K_{ij} , and give rise to spin liquids and dimerized states.

Assuming that all microscopic symmetries of the system (space-group, time-reversal, and spin-rotation symmetries) are preserved, all fully symmetric spin-liquid states with U(1) gauge group can be classified by their respective invariant PSG as introduced in Sec. III C 3. On the triangular lattice, restricting to nearest-neighbor hoppings, there are only two distinct fully symmetric spin-liquid states [31,32]:

- (1) The RVB state with uniform real hoppings on every bond, which corresponds to a U(1) spinon Fermi-surface spin liquid.
- (2) The staggered flux state, with an emergent π flux for the spinons in every other triangular plaquette (this can be achieved by purely real hoppings with identical magnitude,

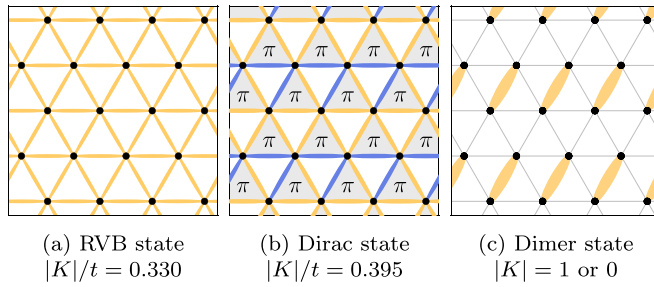


FIG. 5. Visualization of spin-liquid *Ansatz* and dimer states on the moiré triangular lattice at half-filling $\bar{n} = 1$. Orange bonds denote positive spinon hopping amplitudes and, by self-consistency, rotor couplings K_{ij} , while blue bonds denote negative hoppings and couplings. The width of the bonds is in proportion to the amplitude of rotor coupling $K_{ij} = \sum_{\sigma} \langle f_{i,\sigma}^{\dagger} f_{j,\sigma}^{\dagger} \rangle$ on the respective bond. In all cases, $\mu = 0$, $U/t = 10$, $V/U = \frac{1}{4}$, and $V'/V = 1/\sqrt{3}$.

but a particular sign pattern). The spinon spectrum then exhibits Dirac nodes, and the spin state corresponds to a U(1) Dirac spin liquid.

Restricting to particular representative (gauge-fixed) *Ansatz* states, we find that both the RVB state and staggered flux states are solutions to our self-consistency equations. The form of the rotor coupling as well as spinon hopping parameters (which are proportional in magnitude to each other following the perturbative calculation in Sec. III C 2) as a result from the self-consistency calculation are shown in Figs. 5(a) and 5(b). For the RVB *Ansatz* state (i), with the gauge choice commensurate with the full translational symmetry of the triangular lattice, there is a single band and at the self-consistent point the effective spinon Fermi energy $\varepsilon_F = h + \mu$ implies that the system is half-filled. The band structure is shown in Fig. 6. For the staggered flux state (ii), the translational symmetry is realized projectively such that any gauge-fixed configuration of hopping parameters requires two inequivalent sites and a doubling of the unit cell to accommodate the flux pattern. As a result, there are two

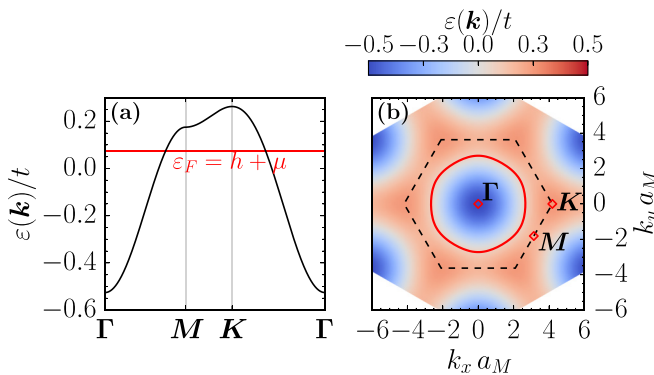


FIG. 6. Spinon band structure of the 0-flux RVB state on the moiré triangular lattice, for $\mu = 0$, $U/t = 10$, $V/U = \frac{1}{4}$, and $V'/V = 1/\sqrt{3}$. The hopping is renormalized by the rotor coupling. (a) Cut along high-symmetry lines. (b) Plot of spinon band in the two-dimensional (hexagonal, dashed) Brillouin zone, with the red circle denotes the spinon Fermi surface. a_M denotes the lattice constant of the triangular moiré superlattice.

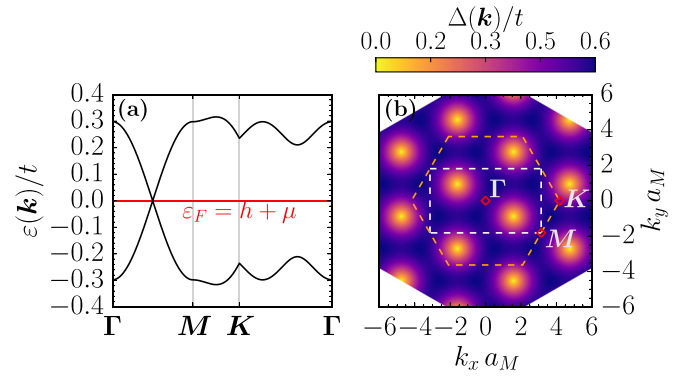


FIG. 7. Spinon band structure of the Dirac state on triangular lattice (lattice constant a_M), for $\mu = 0$, $U/t = 10$, $V/U = \frac{1}{4}$, and $V'/V = 1/\sqrt{3}$. (a) Cut along high-symmetry lines. (b) Energy difference $\Delta(\mathbf{k})/t$ between highest filled and lowest unoccupied band as a function of momentum. The orange hexagon denotes the Brillouin zone of the original triangular lattice, and the white rectangle denotes the Brillouin zone after doubling the unit cell.

bands featuring two Dirac points in the Brillouin zone for the doubled unit cell. The corresponding band structure is shown in Fig. 7.

Allowing for the spontaneous breaking of the lattice's rotational symmetries, additional states can be solutions to the self-consistency equations. For example, an effective (anisotropic) square lattice can form if $K_{ij} = 0$ on all bonds along a certain direction (say, along \hat{x}). The spinon dispersion develops again Dirac points if there is a π -flux in each effective square plaquette.

To find the ground state, we compare the total mean-field energies of various *Ansatz* states. Throughout the half-filled insulating state, dimer states have the lowest energy, as shown explicitly for selected cuts through parameter space in Fig. 4. This is in accord with previous studies that found dimer phases as the mean-field ground states, with a projection back to physical Hilbert space and/or inclusion of gauge fluctuations capable of stabilizing spin-liquid states [33,34]. We leave a systematic investigation of gauge fluctuations of discussed mean-field states for future study.

The energetic competition of the metallic state, the trivial atomic insulator (without any spin correlations) as well as the insulators with spin-dimer and spin-liquid states is shown at chemical potential $\mu = 0$ in Fig. 4. Upon increasing U , the system enters the dimer state before it approaches the atomic insulator (the dashed line) at U_C determined by Eq. (29), where $\sqrt{Z_i}$ would vanish continuously. This corresponds to a first-order phase transition since the respective states (dimer and metallic states) exist as solutions (local minima) of the mean-field calculation on the left- and right-hand sides of the transition, i.e., one of the local minima becomes the new global minimum (as opposed to a new local minima emerging at the critical point). The same also applies for honeycomb and kagome charge crystals below. We also find that, even though the dimer state always has the lowest energy, the U(1) Dirac spin-liquid state (staggered flux) is energetically competitive.

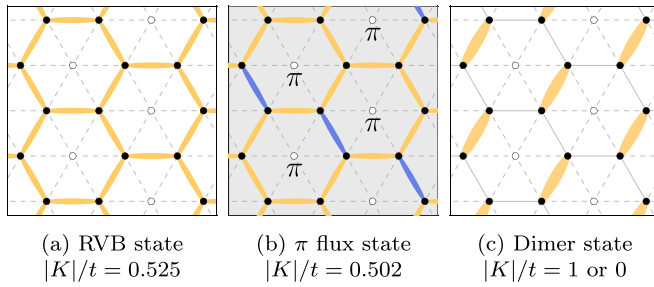


FIG. 8. Visualization of spin-liquid mean-field *Ansatz* and dimer states on the honeycomb Wigner crystal at filling $\bar{n} = \frac{4}{3}$. The color and width of bonds follow the same conventions and normalizations as in Fig. 5. Plaquettes which contain a π flux are shaded gray. In all panels, $\mu/t = 12$, $U/t = 10$, $V/U = \frac{1}{4}$, and $V'/V = 0$.

2. Honeycomb charge crystal ($\frac{4}{3}$ filling)

For some regions in parameter space, effective honeycomb charge crystals are formed, at commensurate $\frac{4}{3}$ filling, where the half-filled sites form an effective honeycomb lattice “stuffed” with doubly occupied sites. While the doubly occupied sites are effectively decoupled from the system as demanded by self-consistency, spinons can hop on the half-filled honeycomb sublattice, which possesses an effective C_{6v} point-group symmetry. There are two fully symmetric U(1) spin-liquid *Ansätze* as classified by the PSG [35]:

- (1) the RVB state, with no emergent flux;
- (2) the π -flux state with a uniform π flux in each hexagonal plaquette.

We display (gauge-fixed) configurations for these two states in Figs. 8(a) and 8(b). For the 0-flux RVB state, the spinon band structure features two Dirac cones as shown in Figs. 9(a) and 9(b). For the π -flux state, the mean-field spinon Hamiltonian requires (at least) a doubling unit cell to accommodate the π flux, and thus the four branches of bands give rise to four Dirac points in the halved Brillouin zone [Figs. 9(c) and 9(d)].

We show the energies of various *Ansatz* states as a function of U/t at chemical potential $\mu/t = 12$ in Fig. 4. Similar to the triangular charge crystal, we find that on the $n = \frac{4}{3}$ charge crystal the dimer state Fig. 8(c) has the lowest energy of all insulating states. (The $n = \frac{5}{3}$ insulator is not shown there, even though it could have the lowest energy as shown in the phase diagram Fig. 3. The same applies for $n = \frac{5}{4}$ kagome charge crystal below.) We further note that the spin-liquid states and the dimer state are close in energy, and the 0-flux RVB spin liquid has a consistently lower energy than the π -flux state.

3. Kagome charge crystal ($\frac{5}{4}$ filling)

Similar to the triangular lattice formed by charges at half-filling, the geometrical frustration of kagome charge crystal is promising for realizing quantum spin-liquid states. Again focusing on U(1) spin liquids, here we consider two spin-liquid states which have been found to be most competitive in energy among all PSG-allowed symmetric spin liquids on kagome lattice [36,37]:

- (1) the RVB state, with no emergent flux in either triangular and hexagonal plaquettes, denoted as $[0,0]$;

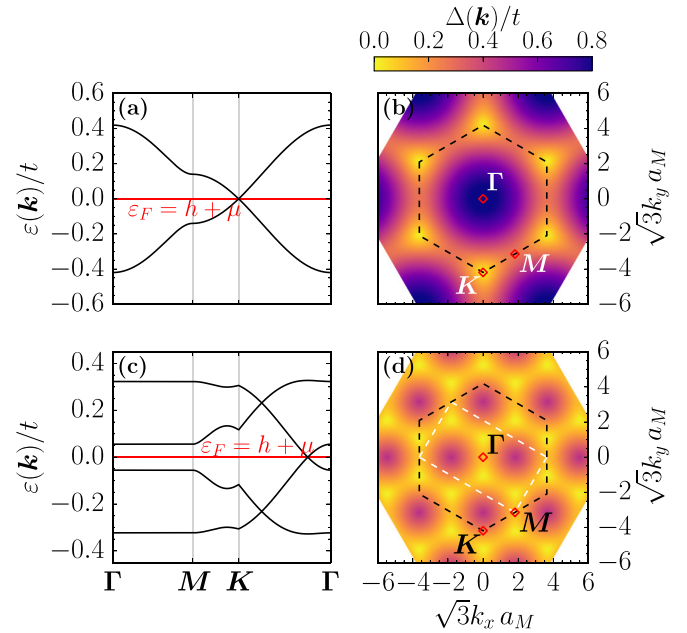


FIG. 9. (a), (b) Same as Fig. 7, but now for the 0-flux RVB state on the honeycomb charge crystal for $\mu/t = 12$, $U/t = 10$, $V/U = \frac{1}{4}$, and $V' = 0$. The dashed hexagon in (b) denotes the Brillouin zone of the honeycomb charge crystal on the moiré triangular lattice, with lattice constant a_M . (c), (d) Same as (a) and (b), but now for the π -flux RVB state on the honeycomb charge crystal (lattice constant a_M) for $\mu/t = 12$, $U/t = 10$, $V/U = \frac{1}{4}$, and $V' = 0$. The white rectangle in (d) denotes that of the doubled unit cell with four Dirac points at the spinon Fermi level.

- (2) the Dirac state with zero flux on triangular plaquettes, but π flux on hexagonal plaquettes, denoted as $[0,\pi]$.

We illustrate the mean-field *Ansätze*, corresponding to particular gauge-fixed configurations, with self-consistent parameters in Figs. 10(a) and 10(b).

The spinon band structure of the RVB $[0,0]$ state (corresponding to uniform hopping of spinons on the emergent kagome lattice) is shown in Fig. 11. The topmost band is found to be exactly flat corresponding to localized modes on the hexagonal plaquettes of the kagome lattice [38], and there are two Dirac points at the K/K' corners of the Brillouin zone. The spinon Fermi level $\varepsilon_F = h + \mu$ lies away from the Dirac

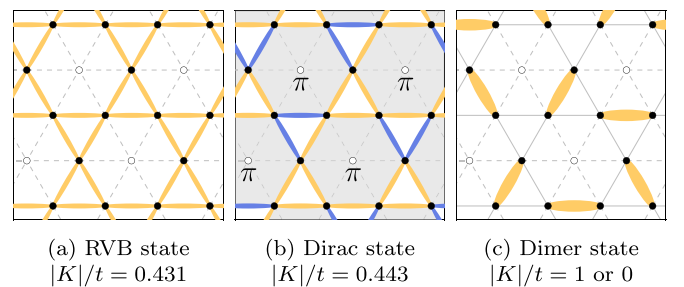


FIG. 10. Visualization of mean-field spin-liquid *Ansatz* and dimer states for kagome charge crystal at filling $\bar{n} = \frac{5}{4}$. The color and width of bonds have the same normalization as in Fig. 5. In all cases, $\mu/t = 12$, $U/t = 10$, $V/U = \frac{1}{4}$, and $V'/V = 1/\sqrt{3}$.

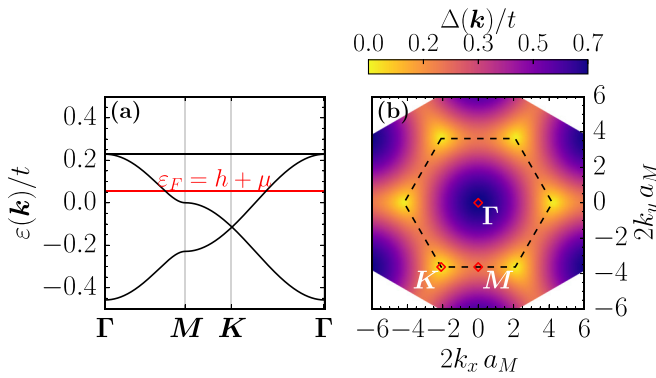


FIG. 11. Same as Fig. 7, but now for the RVB $[0,0]$ state on the kagome charge crystal (lattice constant a_M) at $\mu/t = 12$, $U/t = 10$, $V/U = \frac{1}{4}$, and $V'/V = 1/\sqrt{3}$. (a) Cut along high-symmetry path. (b) The dashed hexagon denotes the Brillouin zone of kagome charge crystal with Dirac points at K/K' .

points in order to enforce half-filling of the spinon bands, such that the RVB $[0,0]$ state corresponds to a $U(1)$ spinon Fermi-surface spin liquid. We now turn to the Dirac $[0,\pi]$ state, for which a doubling of unit cell is needed to accommodate a mean-field parameter configuration that contains a π flux on hexagonal plaquettes. The resulting band structure features a twofold-degenerate flat band, as shown in Fig. 12, and there are two Dirac points at the spinon Fermi level $\varepsilon_F = \mu + h$.

However, similar to the previously discussed case of the triangular lattice with unit occupancy, we find that through the phase diagram, spin-dimer states (on top of the kagome charge crystal) have a lower mean-field energy than the two symmetric spin-liquid Ansätze described previously. An example of such a dimer configuration is shown in Fig. 10(c). The energies of different candidate states on the kagome Wigner crystal are shown in Fig. 4(c). Note that within the insulating phase, the $U(1)$ Dirac $[0,\pi]$ spin liquid is most competitive in energy to spin-dimer states, while the RVB $[0,0]$ spin liquid

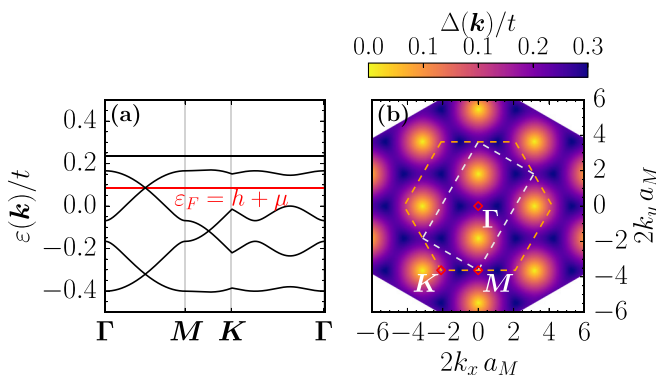


FIG. 12. Same as Fig. 7, but now for the Dirac $[0,\pi]$ state on the kagome charge crystal (lattice constant a_M), for $\mu/t = 12$, $U/t = 10$, $V/U = \frac{1}{4}$, and $V'/V = 1/\sqrt{3}$. (a) Cut along high-symmetry path. Note that the top flat band is twofold degenerate. (b) The dashed hexagon denotes the Brillouin zone of the kagome charge crystal, and the white rectangle denotes the Brillouin zone after doubling the unit cell, containing two Dirac points at the Fermi level.

and trivial insulator (without any spinon hopping or hybridization) are higher in energy.

V. BEYOND MEAN-FIELD THEORY: STABILITY AND EXPERIMENTAL DETECTION

A. Spin liquids on triangular charge crystal

Our results indicate that on the triangular lattice, the $U(1)$ Dirac spin liquid that occurs with a staggered π -flux background is the energetically most preferred spin-liquid Ansatz state. This is in accord with theoretical studies of Heisenberg models valid deep in the insulating state [32,39], though a $U(1)$ spinon Fermi-surface state has also been considered a strong candidate in Hubbard models [40,41]. At low energies, the $U(1)$ Dirac spin liquid is described by quantum electrodynamics in 2+1 dimensions (QED_3), where the $SU(2)_{\text{pseudospin}} \times SU(2)_{\text{valley}}$ symmetry is enhanced to an emergent $SU(4)$ symmetry. QED_3 is believed to be stable and flow to an infrared fixed point with conformal symmetry [4,42]. A key consequence of this low-energy conformal field theory (CFT) is that correlation functions of order parameters close to the QED_3 fixed-point theory are expected to fall off as anomalous power laws. For example, spin-spin correlation functions will be dominated by

$$\langle S^\alpha(\mathbf{x})S^\beta(\mathbf{y}) \rangle \sim \frac{e^{-i\mathbf{K}_m \cdot (\mathbf{x}-\mathbf{y})}}{|\mathbf{x}-\mathbf{y}|^{2\Delta_\phi}} + \text{H.c.} + \dots, \quad (31)$$

where $\Delta_\phi \approx 1.02$ is the scaling dimension of the monopole operator in the QED_3 CFT according to latest bootstrap studies [43,44], and \mathbf{K}_m denotes a wave vector at the corner of the hexagonal moiré Brillouin zone. Here, we stress that in the context of moiré TMD discussed in this paper, the spin operators $S^\alpha(\mathbf{r})$ in Eq. (31) refer to the $SU(2)$ spin-valley pseudospin degree of freedom associated with a charge carrier.

We briefly comment on experimental signatures of this putative spin-liquid state in the context of moiré heterostructures. While these systems are not amenable to conventional probes of magnetism and magnetic order such as neutron scattering due to limited sample sizes, their two-dimensional nature allows them to be readily integrated into two-dimensional tunnel junctions. Following experimental works on tunneling spectroscopy of magnons in van der Waals magnets [45] as well as a theoretical proposal by Koenig *et al.* [46], we suggest that the anomalous pseudospin correlations in Eq. (31) of the putative Dirac spin liquid could be probed using inelastic tunneling spectroscopy, where electrons tunneling between two planar metallic substrates at the top and bottom of the heterostructure scatter off spin excitations in the moiré TMD system. Adopting the scaling arguments of Ref. [46], the inelastic contribution $I_{\text{inel.}}$ to the tunneling current $I = I_{\text{el.}} + I_{\text{inel.}}$ would then exhibit an anomalous differential conductance $dI_{\text{inel.}}/dV \sim V^{2\Delta_\phi-1}$ with Δ_ϕ as introduced in Eq. (31). As a comparison, for the Heisenberg 120° antiferromagnet with linearly dispersing magnons, one would expect $dI_{\text{inel.}}/dV \sim V^2$. However, we note that energy and temperature scales at which these universal power laws are expected to be observable are unclear as of now.

B. Spin liquids on honeycomb charge crystal

We comment that U(1) spin-liquid states with spinons dispersing on an effective honeycomb lattice formed by localized charges will in general be *unstable*. There are two main mechanisms for their instability.

On the one hand, we note that the gapless Dirac cone in the spinon dispersion in this state is protected by a combination of time-reversal and inversion symmetries. As discussed in Sec. II B, the inversion symmetry of moiré-Hubbard model on the triangular lattice occurs as an artifact of truncating the Fourier expansion of the moiré potentials $\Delta_{\pm}(\mathbf{r})$ and $\Delta_T(\mathbf{r})$ beyond leading order. Accounting for higher-order harmonics, this symmetry is broken and thus the spinon Dirac cones can be gapped out by terms of microscopic origin. Hence, an effective field theory that describes this spin-liquid state corresponds to a pure U(1) lattice gauge theory in 2+1 dimensions. However, as shown by Polyakov [26,27], such compact U(1) gauge theory is unstable against monopole proliferation.

On the other hand, even if the spinon Dirac cones are stable, in Ref. [42] it was demonstrated that U(1) Dirac spin liquids on the honeycomb lattice are *unstable* because there exists a monopole excitation that transforms trivially under all microscopic symmetries, and can thus proliferate.

We therefore conclude that the U(1) spin-liquid states for filling $\bar{n} = \frac{4}{3}$ are in general not expected to be stable against monopole proliferation, likely giving way to confined states such as magnetically ordered or dimer states.

C. Spin liquids on the kagome charge crystal

Amongst pure Heisenberg spin models, the kagome lattice antiferromagnet has long been known to have the strongest tendency to avoid magnetic ordering. While there is consensus on this point from many calculations, the precise nature of the nonmagnetic ground state, and its sensitivity to weak interactions beyond nearest-neighbor exchange, are under debate. Spontaneously dimerized valence bond solid states [47], as well as U(1) Dirac [36,37,42] and \mathbb{Z}_2 [48–51] spin-liquid states are competitive energetically.

We may therefore expect a spin liquid to obtain as well for the kagome charge crystal. Within our framework, we find that the most competitive spin-liquid state is a U(1) Dirac state, which is in accord with variational wave-function studies for the aforementioned Heisenberg models. The experimental signatures of a such a state would be similar to those discussed above for the triangular lattice Mott insulator.

D. Dimer states

For all charge crystals, forming effective triangular, honeycomb, and kagome lattices, within our mean-field theory we saw that dimerized states are actually more favorable than spin liquids and cannot be discounted. At the mean-field level, these dimer states retain a very high degeneracy, associated to the positioning of the dimers. This degeneracy is an artifact of the mean-field treatment and is not expected to be exact. Instead, perturbative corrections in K/U beyond the mean-field approximation will induce energy differences between different dimer configurations, tending to stabilize particular dimer coverings of the lattice. More generally, one might

invoke an effective dimer model to describe the dynamics and state selection within the space of singlet dimer coverings. Typically, the “potential” terms within such a dimer model tend to induce an ordered configuration of singlet bonds, i.e., a valence bond crystal. A gapped \mathbb{Z}_2 resonating valence bond spin-liquid state is also conceivable, if the “kinetic” terms of such an effective dimer model dominate.

Valence bond solid states thus appear highly plausible, and should be detectable experimentally if present. They can occur *a priori* not only in the kagome charge crystal but also for other insulating fillings. While the precise pattern of ordered dimers in such a state is hard to predict, a number of candidates have been discussed in the literature. Rather than trying to differentiate amongst many different possible orderings, here we point out that at the grossest level they all share commonalities which suggest similar experimental signatures. In particular, any dimer pattern necessarily breaks discrete space-group symmetries. Consequently, a valence bond solid state exhibits domains and domain walls, and moreover the domains couple to lattice deformations. These facts tend to lead to substantial *increases* in resistance when such symmetry breaking occurs, for example, from the difficulty of propagating electrons across domain walls, against preferred directions, and from opening of gaps. In other metals with discrete symmetry breaking these resistivity enhancements can be quite dramatic [52,53]. In twisted TMDs, we can expect valence bond solid states to show similar resistivity enhancements tuned by gating and applied fields. If the dimer order breaks rotational symmetry, that may also be detectable directly in transport, as it has been in nematic quantum Hall states.

VI. SUMMARY AND OUTLOOK

In this paper, we have studied the triangular moiré-Hubbard model as an effective model for correlated states in moiré heterobilayers and twisted homobilayers of transition metal dichalcogenides. Motivated by the experimental discovery of self-organized charge lattices (generalized Wigner crystals) at various filling factors, we have employed a self-consistent slave-rotor mean-field theory to map out phase diagrams containing both insulating states as well as metallic (compressible) states as a function of interaction strength and filling, reproducing several experimentally found charge-ordering patterns, where we point out that longer-ranged (next-nearest-neighbor) repulsive interactions are crucial for the stabilization of kagome-type charge crystals.

By splitting electronic quasiparticles into charge rotor and fermionic spinon degrees of freedom, the slave-rotor mean-field theory (upon including charge fluctuations perturbatively) allows us to study spin states on top of the charge-ordered background, possibly including exotic spin-liquid states. Such states are expected if the generalized Wigner crystals form *frustrated* lattices, which occurs at half-filling (corresponding to a triangular lattice), as well as at filling $\bar{n} = \frac{5}{4}$, where kagome-type lattices are stabilized.

Among all candidate *Ansatz* states, we find that *on the mean-field level*, dimer states are always energetically preferred, but certain spin liquids are found to have competitive

energies, and may be realized as ground states in certain parameter regimes after accounting for gauge fluctuations and Gutzwiller projection. We discuss the stability of these states, as well as means of experimental detection of spin liquids and dimer states that are particularly suitable for two-dimensional heterostructures. In the future, it would be ideal to improve the quantitative accuracy of this study by elevating the mean-field approximation to variational status via suitable wave functions. At present we simply assert that the current method qualitatively captures the physics of charge ordering, bandwidth and mass renormalization, and possible spin-liquid and dimer states.

We note that we have restricted our study to dimer states as well as *symmetric* U(1) spin liquids, which are necessarily gapless. While these states have previously been found to be prime contenders for spin-liquid ground states of frustrated Heisenberg models on the triangular and kagome lattices [32], \mathbb{Z}_2 spin-liquid states cannot be ruled out *a priori*. Indeed, there are feasible DMRG calculations supporting a gapped \mathbb{Z}_2 spin liquid in triangular lattice Heisenberg models [54,55]. Moreover, DMRG studies of the triangular lattice Hubbard model have suggested that virtual charge fluctuations at intermediate values of t/U may stabilize gapped chiral spin liquids (CSL) [56,57]. In a similar vein, one may consider vertical displacement fields which explicitly break the $SU(2)_{\text{pseudospin}}$ degeneracy of the moiré-Hubbard model [5], leading to Dzyaloshinskii-Moriya interactions in effective spin models obtained at large t/U . These interactions have been suggested to induce noncollinear magnetic order as well as chiral spin-liquid phases [17,58]. As for kagome charge order ($\frac{5}{4}$ filling), recent DMRG [17] and Schwinger boson [59] studies have suggested the possibility of chiral spin-liquid phases on kagome lattice. A highly interesting extension of our work therefore consists in allowing for spontaneous breaking of time-reversal symmetry, which could capture possible CSL phases as well as (possibly complex) magnetic order, which we have explicitly excluded out in the paper at hand.

On the experimental front, we remark that detection of magnetic long-range order in moiré TMD heterostructure is still at its infancy. Recently, first evidence for ferromagnetic long-range order in *R*-stacked MoTe₂ was provided [60]. While there are signatures of antiferromagnetic *interactions*,

for example, in WSe₂/WS₂, both at half-filling [7] as well as fractional filling [61], no direct detection of antiferromagnetic *long-range order* in moiré TMD has been reported. Establishing new experimental probes for magnetically ordered states in moiré TMD constitutes an important milestone for the eventual realization and detection of quantum dimer or quantum spin-liquid phases in these systems.

ACKNOWLEDGMENTS

We thank J. Cano and L. Rademaker for helpful conversations. U.F.P.S. is supported by the Deutsche Forschungsgemeinschaft (DFG, German Research Foundation) through a Walter Benjamin fellowship, Project ID No. 449890867. Z.X.L. is supported by the Simons Collaborations on Ultra-Quantum Matter, Grant No. 651440 from the Simons Foundation. L.B. and Z.S. were supported by the DOE, Office of Science, Basic Energy Sciences under Award No. DE-FG02-08ER46524, and by the Simons Collaboration on Ultra-Quantum Matter, which is a grant from the Simons Foundation (Grant No. 651440). This work was performed in part at the Aspen Center for Physics, which is supported by National Science Foundation Grant No. PHY-2210452.

APPENDIX A: ACCIDENTAL SYMMETRY OF MOIRÉ-HUBBARD MODELS

Here, we show that the effective Hamiltonian of Ref. [5] for the twisted homobilayer exhibits an accidental symmetry. Moiré bands and wave functions are obtained as solutions to the Schrödinger equation $\mathcal{H}\psi = E\psi$ where

$$\mathcal{H} = \begin{pmatrix} -\frac{1}{2m}(\hat{\mathbf{k}} - \boldsymbol{\kappa}_+)^2 + \Delta_+(\mathbf{r}) & \Delta_T(\mathbf{r}) \\ \Delta_T^\dagger(\mathbf{r}) & -\frac{1}{2m}(\hat{\mathbf{k}} - \boldsymbol{\kappa}_-)^2 + \Delta_-(\mathbf{r}) \end{pmatrix}, \quad (\text{A1})$$

where $\hat{\mathbf{k}} = -i\nabla$ is the momentum operator acting in real space, and $\Delta_\pm(\mathbf{r})$ and $\Delta_T(\mathbf{r})$ are moiré potentials in each layer and the interlayer tunneling, respectively. If the Bloch *Ansatz* $\psi = e^{i\mathbf{k}\cdot\mathbf{r}}u_{\mathbf{k}}(\mathbf{r})$ solves the Schrödinger equation with energy $E_{\mathbf{k}}$, the Bloch wave function $w_{\mathbf{k}'}(x, y) \equiv (u_{\mathbf{k}}(x, -y))^*$ with $\mathbf{k}' = (-k_x, k_y)$ solves

$$\begin{pmatrix} -\frac{1}{2m}(\hat{\mathbf{k}} + \mathbf{k} + \boldsymbol{\kappa}_-)^2 + \Delta_+(x, -y) & \Delta_T^\dagger(x, -y) \\ \Delta_T(x, -y) & -\frac{1}{2m}(\hat{\mathbf{k}} + \mathbf{k} + \boldsymbol{\kappa}_+)^2 + \Delta_-(x, -y) \end{pmatrix} w_{\mathbf{k}'} = E_{\mathbf{k}'} w_{\mathbf{k}'}, \quad (\text{A2})$$

where we use that $\Delta_\pm(\mathbf{r})$ is real. Since $\boldsymbol{\kappa}_+ + \boldsymbol{\kappa}_-$ is equal to a reciprocal lattice vector, we can write $w_{\mathbf{k}'} = \tilde{w}_{\mathbf{k}'} e^{-i(\boldsymbol{\kappa}_+ + \boldsymbol{\kappa}_-)\cdot\mathbf{r}}$.

Now, if we assume that $\Delta_\pm(x, -y) = \Delta_\pm(x, y)$ and $\Delta_T(x, -y) = \Delta_T^\dagger(x, y)$, the resulting Bloch problem for $\tilde{w}_{\mathbf{k}'}$, with energy $E_{\mathbf{k}'}$ takes the same form as $u_{\mathbf{k}}$ with eigenvalue $E_{\mathbf{k}}$. Hence, there exists a combination of time-reversal and reflection symmetries that relates

$$u_{\mathbf{k}'}(x, y) = e^{i(\boldsymbol{\kappa}_1 + \boldsymbol{\kappa}_2)\cdot\mathbf{r}} u_{\mathbf{k}}^*(x, -y). \quad (\text{A3})$$

Crucially, this symmetry requires $\Delta_\pm(x, -y) = \Delta_\pm(x, y)$ and $\Delta_T(x, -y) = \Delta_T^\dagger(x, y)$, which is satisfied by general moiré

potentials only if their Fourier coefficients are restricted to the first shell of reciprocal lattice vectors.

In the case of heterobilayers with strong band offsets [20], the moiré-Bloch spectrum is derived by solving the Schrödinger equation for a valence band hole, $\mathcal{H} = \kappa\kappa^2/(2m) + V(\mathbf{x})$, where $V(\mathbf{x})$ is the moiré potential which can be extracted from DFT simulations. Keeping the C_3 symmetry manifest and expanding $V(\mathbf{x})$ to include only the first harmonics (i.e., reciprocal lattice vectors only in the first moiré-Brillouin zone) leads to a spurious reflection symmetry, which is broken explicitly upon keeping higher-order terms in the expansion of $V(\mathbf{x})$.

APPENDIX B: LONGER-RANGED REPULSIVE INTERACTIONS AND WIGNER CRYSTALLIZATION

While the (screened) Coulomb repulsion in moiré heterostructures is generally long ranged, it is easier for theoretical analysis and qualitative insights to truncate repulsive interactions between n th nearest neighbors on the effective moiré triangular lattice. However, we point out that such truncated models might not exhibit more complex charge-ordered (Wigner lattice) as stable thermodynamic ground states. As a particular example, we consider the moiré-Hubbard model of Eq. (1). At $t = 0$, charges do not possess any dynamics and for filling $n \geq 1$, we can map the Hamiltonian onto an effective Ising model with $s_i = 2n_i - 3$ such that $s_i = +1$ (-1) corresponds to doubly occupied (singly occupied) sites (a similar mapping can be performed for fillings $n < 1$). Then, the effective Hamiltonian $H = H_U + H_\mu$ with $H_\mu = -\mu \sum_i n_i$ can be written as

$$H = J \sum_{\langle ij \rangle} s_i s_j - h \sum_i s_i, \quad (\text{B1})$$

which corresponds to an antiferromagnetic Ising model on the triangular lattice with nearest-neighbor coupling $J = V/4 > 0$ and a longitudinal field $h = (U + 6V + \mu)/2$.

As is well known, the antiferromagnetic Ising model possesses an extensive degeneracy at zero field $h = 0$, which is lifted by any infinitesimal $|h| > 0$ in favor of a state with $m^z = \pm \frac{1}{3}$ magnetization, which corresponds precisely to the $\sqrt{3} \times \sqrt{3}$ Wigner crystal states forming an effective honeycomb lattice with singly occupied and doubly occupied states. Further increasing h , at $|h| = 6J$ saturation is achieved, with all Ising spins pointing up and down (corresponding to the trivial band insulator of doubly occupied sites, or the half-filled triangular lattice).

Importantly, this argument implies that the kagome charge crystal with filling $\bar{n} = \frac{5}{4}$ does not exist in the grand-canonical ensemble if only nearest-neighbor repulsion is taken into account, and such that finite $V' \neq 0$ is required to stabilize the Wigner crystal states.

-
- [1] R. Bistritzer and A. H. MacDonald, *Proc. Natl. Acad. Sci. USA* **108**, 12233 (2011).
- [2] Y. Cao, V. Fatemi, S. Fang, K. Watanabe, T. Taniguchi, E. Kaxiras, and P. Jarillo-Herrero, *Nature (London)* **556**, 43 (2018).
- [3] Y. Cao, V. Fatemi, A. Demir, S. Fang, S. L. Tomarken, J. Y. Luo, J. D. Sanchez-Yamagishi, K. Watanabe, T. Taniguchi, E. Kaxiras, R. C. Ashoori, and P. Jarillo-Herrero, *Nature (London)* **556**, 80 (2018).
- [4] Z.-D. Song and B. A. Bernevig, *Phys. Rev. Lett.* **129**, 047601 (2022).
- [5] H. Pan, F. Wu, and S. Das Sarma, *Phys. Rev. Res.* **2**, 033087 (2020).
- [6] H. Pan, F. Wu, and S. Das Sarma, *Phys. Rev. B* **102**, 201104(R) (2020).
- [7] Y. Tang, L. Li, T. Li, Y. Xu, S. Liu, K. Barmak, K. Watanabe, T. Taniguchi, A. H. MacDonald, J. Shan, and K. F. Mak, *Nature (London)* **579**, 353 (2020).
- [8] D. M. Kennes, M. Claassen, L. Xian, A. Georges, A. J. Millis, J. Hone, C. R. Dean, D. N. Basov, A. N. Pasupathy, and A. Rubio, *Nat. Phys.* **17**, 155 (2021).
- [9] A. Wietek, J. Wang, J. Zang, J. Cano, A. Georges, and A. Millis, *Phys. Rev. Res.* **4**, 043048 (2022).
- [10] F. Wu, T. Lovorn, E. Tutuc, I. Martin, and A. H. MacDonald, *Phys. Rev. Lett.* **122**, 086402 (2019).
- [11] Z. Tao, B. Shen, W. Zhao *et al.*, *Nat. Nanotechnol.* (2023).
- [12] J. Cai, E. Anderson, C. Wang, X. Zhang, X. Liu, W. Holtzmann, Y. Zhang, F. Fan, T. Taniguchi, K. Watanabe, Y. Ran, T. Cao, L. Fu, D. Xiao, W. Yao, and X. Xu, *Nature (London)* **622**, 63 (2023).
- [13] Y. Zeng, Z. Xia, K. Kang, J. Zhu, P. Knüppel, C. Vaswani, K. Watanabe, T. Taniguchi, K. F. Mak, and J. Shan, *arXiv:2305.00973*.
- [14] E. C. Regan, D. Wang, C. Jin, M. I. Bakti Utama, B. Gao, X. Wei, S. Zhao, W. Zhao, Z. Zhang, K. Yumigeta, M. Blei, J. D. Carlström, K. Watanabe, T. Taniguchi, S. Tongay, M. Crommie, A. Zettl, and F. Wang, *Nature (London)* **579**, 359 (2020).
- [15] H. Li, S. Li, E. C. Regan, D. Wang, W. Zhao, S. Kahn, K. Yumigeta, M. Blei, T. Taniguchi, K. Watanabe, S. Tongay, A. Zettl, M. F. Crommie, and F. Wang, *Nature (London)* **597**, 650 (2021).
- [16] N. C. Hu and A. H. MacDonald, *Phys. Rev. B* **104**, 214403 (2021).
- [17] J. Motruk, D. Rossi, D. A. Abanin, and L. Rademaker, *Phys. Rev. Res.* **5**, L022049 (2023).
- [18] L. Savary and L. Balents, *Rep. Prog. Phys.* **80**, 016502 (2017).
- [19] C. Broholm, R. J. Cava, S. A. Kivelson, D. G. Nocera, M. R. Norman, and T. Senthil, *Science* **367**, eaay0668 (2020).
- [20] F. Wu, T. Lovorn, E. Tutuc, and A. H. MacDonald, *Phys. Rev. Lett.* **121**, 026402 (2018).
- [21] U. F. P. Seifert and L. Balents, *arXiv:2304.13068*.
- [22] S. Florens and A. Georges, *Phys. Rev. B* **70**, 035114 (2004).
- [23] L. Wang, E.-M. Shih, A. Ghiotto, L. Xian, D. A. Rhodes, C. Tan, M. Claassen, D. M. Kennes, Y. Bai, B. Kim, K. Watanabe, T. Taniguchi, X. Zhu, J. Hone, A. Rubio, A. N. Pasupathy, and C. R. Dean, *Nat. Mater.* **19**, 861 (2020).
- [24] T. Devakul, V. Crépel, Y. Zhang, and L. Fu, *Nat. Commun.* **12**, 6730 (2021).
- [25] X.-G. Wen, *Phys. Rev. B* **65**, 165113 (2002).
- [26] A. Polyakov, *Phys. Lett. B* **59**, 82 (1975).
- [27] A. M. Polyakov, *Nucl. Phys. B* **120**, 429 (1977).
- [28] K. F. Mak and J. Shan, *Nat. Nanotechnol.* **17**, 686 (2022).
- [29] T. Li, J. Zhu, Y. Tang, K. Watanabe, T. Taniguchi, V. Elser, J. Shan, and K. F. Mak, *Nat. Nanotechnol.* **16**, 1068 (2021).
- [30] Y. Xu, S. Liu, D. A. Rhodes, K. Watanabe, T. Taniguchi, J. Hone, V. Elser, K. F. Mak, and J. Shan, *Nature (London)* **587**, 214 (2020).
- [31] Y.-M. Lu, *Phys. Rev. B* **93**, 165113 (2016).
- [32] Y. Iqbal, W.-J. Hu, R. Thomale, D. Poilblanc, and F. Becca, *Phys. Rev. B* **93**, 144411 (2016).
- [33] M. B. Hastings, *Phys. Rev. B* **63**, 014413 (2000).

- [34] D. S. Rokhsar, *Phys. Rev. B* **42**, 2526 (1990).
- [35] F. Wang, *Phys. Rev. B* **82**, 024419 (2010).
- [36] Y. Ran, M. Hermele, P. A. Lee, and X.-G. Wen, *Phys. Rev. Lett.* **98**, 117205 (2007).
- [37] Y. Iqbal, F. Becca, and D. Poilblanc, *Phys. Rev. B* **84**, 020407(R) (2011).
- [38] D. L. Bergman, C. Wu, and L. Balents, *Phys. Rev. B* **78**, 125104 (2008).
- [39] S. Hu, W. Zhu, S. Eggert, and Y.-C. He, *Phys. Rev. Lett.* **123**, 207203 (2019).
- [40] O. I. Motrunich, *Phys. Rev. B* **72**, 045105 (2005).
- [41] S.-S. Lee and P. A. Lee, *Phys. Rev. Lett.* **95**, 036403 (2005).
- [42] X.-Y. Song, C. Wang, A. Vishwanath, and Y.-C. He, *Nat. Commun.* **10**, 4254 (2019).
- [43] E. Dyer, M. Mezei, and S. S. Pufu, *arXiv:1309.1160*.
- [44] S. Albayrak, R. S. Erramilli, Z. Li, D. Poland, and Y. Xin, *Phys. Rev. D* **105**, 085008 (2022).
- [45] D. R. Klein, D. MacNeill, J. L. Lado, D. Soriano, E. Navarro-Moratalla, K. Watanabe, T. Taniguchi, S. Manni, P. Canfield, J. Fernández-Rossier, and P. Jarillo-Herrero, *Science* **360**, 1218 (2018).
- [46] E. J. König, M. T. Randeria, and B. Jäck, *Phys. Rev. Lett.* **125**, 267206 (2020).
- [47] R. R. P. Singh and D. A. Huse, *Phys. Rev. B* **76**, 180407(R) (2007).
- [48] F. Wang and A. Vishwanath, *Phys. Rev. B* **74**, 174423 (2006).
- [49] S. Yan, D. A. Huse, and S. R. White, *Science* **332**, 1173 (2011).
- [50] Y.-M. Lu, Y. Ran, and P. A. Lee, *Phys. Rev. B* **83**, 224413 (2011).
- [51] S. Depenbrock, I. P. McCulloch, and U. Schollwöck, *Phys. Rev. Lett.* **109**, 067201 (2012).
- [52] T. Suzuki, L. Savary, J.-P. Liu, J. W. Lynn, L. Balents, and J. G. Checkelsky, *Science* **365**, 377 (2019).
- [53] R. A. Borzi, S. A. Grigera, J. Farrell, R. Perry, S. Lister, S. Lee, D. Tennant, Y. Maeno, and A. P. Mackenzie, *Science* **315**, 214 (2007).
- [54] W.-J. Hu, S.-S. Gong, W. Zhu, and D. N. Sheng, *Phys. Rev. B* **92**, 140403(R) (2015).
- [55] Z. Zhu and S. R. White, *Phys. Rev. B* **92**, 041105(R) (2015).
- [56] A. Szasz, J. Motruk, M. P. Zaletel, and J. E. Moore, *Phys. Rev. X* **10**, 021042 (2020).
- [57] T. Cookmeyer, J. Motruk, and J. E. Moore, *Phys. Rev. Lett.* **127**, 087201 (2021).
- [58] L. Messio, S. Bieri, C. Lhuillier, and B. Bernu, *Phys. Rev. Lett.* **118**, 267201 (2017).
- [59] D. Rossi, J. Motruk, L. Rademaker, and D. A. Abanin, *arXiv:2305.15824*.
- [60] E. Anderson, F.-R. Fan, J. Cai, W. Holtzmann, T. Taniguchi, K. Watanabe, D. Xiao, W. Yao, and X. Xu, *Science* **381**, 325 (2023).
- [61] Y. Tang, K. Su, L. Li, Y. Xu, S. Liu, K. Watanabe, T. Taniguchi, J. Hone, C.-M. Jian, C. Xu, K. F. Mak, and J. Shan, *Nat. Nanotechnol.* **18**, 233 (2023).